# Formation and atomic structure of ordered Sr-induced nanostrips on Ge(100)

Boris R. Lukanov,[1,2] Kevin F. Garrity,[1,3,4] Sohrab Ismail-Beigi,[1,3] and Eric I. Altman[1,5,*]

[1]*Center for Research on Interface Structures and Phenomena (CRISP), Yale University, New Haven, Connecticut 06520, USA*

[2]*Department of Mechanical Engineering and Materials Science, Yale University, New Haven, Connecticut 06520, USA*

[3]*Department of Applied Physics, Yale University, New Haven, Connecticut 06520 USA*

[4]*Department of Physics and Astronomy, Rutgers University, Piscataway, New Jersey 08854, USA*

[5]*Department of Chemical and Environmental Engineering, Yale University, New Haven, Connecticut 06520, USA*

(Received 10 February 2014; revised manuscript received 8 April 2014; published 29 April 2014)

The deposition of alkaline earths onto Ge(100) surfaces leads to well-ordered arrays of narrow trenches and elongated plateaus that extend for thousands of angstroms. Using scanning tunneling microscopy (STM) in conjunction with density functional theory (DFT), the atomic scale details of these nanostructures are revealed and the driving force responsible for their formation is evaluated. The STM data reveal a dramatic contrast reversal when the polarity of the imaging bias is switched. An energetically favorable structure for the plateaus was found using DFT that can reproduce all of the observed features. This structure is based upon a double dimer vacancy model in which Sr atoms displace two Ge dimers from the surface. Interestingly, the ordered plateau-trench structure is unique to Ge(100) despite the structural and chemical similarities to the Si(100) surface.

DOI: 10.1103/PhysRevB.89.155319 PACS number(s): 68.37.Ef, 68.35.bg, 68.55.A−, 73.20.At

## I. INTRODUCTION

Semiconductor (100) surfaces are the backbone of the modern electronics industry. The Si(100) surface is the universal platform for device architecture, whereas Ge(100) is becoming increasingly important in high-speed technological applications (Si-Ge alloys and strained Ge) due to Ge's higher carrier mobility [1–4]. Growth on Ge(100) has also garnered attention due to the observation that metal deposition onto Ge(100) often leads to self-organization of the metal atoms into one-dimensional (1D) nanowires [5–14]. Interestingly, depositing the same metals onto the nearly identical Si(100) surface does not lead to similar structures [15,16], suggesting that the subtle interplay of surface energetics and metal-substrate interactions tilts the balance in favor of 1D structures on Ge(100). The ability of Ge to promote such structures makes it attractive for applications where self-organization of nanowires and other nanostructures on prepatterned technologically important (100) substrates is desired. This paper focuses on the atomic scale details of alkaline-earth-induced 1D nanostructures on Ge(100).

In addition to the formation of 1D nanostructures, alkaline-earth metal deposition onto Si and Ge(100) is of considerable interest as a crucial first step in the growth of high-quality epitaxial oxide films on these surfaces. Epitaxial crystalline oxides can exhibit a myriad of useful properties ranging from ferroelectricity and ferromagnetism to high-temperature superconductivity, which can impart additional functionalities to conventional semiconductor devices [17–19]. To fully exploit these properties, the interface between the epitaxial film and the substrate needs to be atomically abrupt [20]. Thus far, only a handful of oxides have been grown on semiconductor (100) surfaces that meet this requirement, most notably alkaline-earth oxides and alkaline-earth titanates, e.g., $SrTiO_3$ and $BaTiO_3$ [21,22]. The key to this success has been the initial formation of an atomically ordered alkaline-earth metal submonolayer [21–25]. Depending on temperature, coverage, and substrate material, a number of different surface phases form when alkaline earths are deposited onto semiconductor (100) surfaces [26–29]. Understanding the atomic structure of these phases, how they form, how they template epitaxy while limiting oxidation of the semiconductor, and how they affect the electronic properties of the interface such as density of interface states and band offsets [30–34] is crucial to expanding the number of materials that can be epitaxially grown on semiconductors as well as the range of substrates they can be grown onto.

To advance this goal, we have been studying the growth of alkaline earths on Si and Ge(100) surfaces using scanning tunneling microscopy (STM) complemented by electron diffraction and first-principles density functional theory (DFT) [29,35,36]. In prior work, we showed that a number of ordered phases occur when Ba and Sr are deposited onto Ge(100) including a phase with 1D strips and trenches organized into highly ordered arrays over remarkably long distances [29]. No similar alkaline-earth-induced self-organization of 1D structures has been reported for Si(100).

In this paper, the atomic scale details and driving force for the 1D nanostructures that form when ~3/16 ML (1 monolayer or ML is defined as 1 Sr atom/surface Ge atom) of Sr is deposited on Ge(100) are revealed through comparison of variable-bias STM imaging and first-principles calculations of energetically feasible structures. Given the complexity of the surface morphology and the inherent experimental difficulties in differentiating topographical and electronic contributions to STM data, this combined approach and the good agreement between experimental and simulated STM images was essential to deciphering the surface atomic configurations. We will show that the formation of ordered trenches and plateaus is due to alkaline-earth penetration into the semiconductor surface to form a surface alloy. Differences between Si and Ge are analyzed in terms of differences in their bond lengths with results suggesting that

*Corresponding author: eric.altman@yale.edu

 

Sr can form stable high-coverage phases on Si(100) but not on Ge(100).

## II. METHODS

### A. Experimental Details

Experiments were conducted using an ultrahigh vacuum system equipped with a double-pass cylindrical mirror analyzer for Auger electron spectroscopy (AES), low-energy electron diffraction (LEED) optics, an ion gun, Ge and alkaline-earth sources, a quartz crystal thickness monitor (QCM), and a custom-designed variable-temperature scanning tunneling microscope [35]. The base pressure of the UHV system was maintained in the low $10^{-10}$ Torr range.

Strontium was deposited by resistively heating a Ta coil wrapped around a quartz tube filled with Sr pieces. The deposition rate was kept within 0.15–0.2 ML/min as measured by the QCM. The QCM was calibrated by counting the density of Sr adatoms deposited at room temperature (where all deposited Sr remains on the surface) in STM images. Correlating the room temperature adatom density measurements with the Sr/Ge *LMM* AES peak ratio enabled estimates of the Sr surface atom density at high temperatures where not all of the Sr may remain on the surface.

The Ge(100) samples were cut from an undoped Ge(100) wafer (MTI Corporation) with a resistivity of 55.1–70.5 Ω cm. The surface was heated by conduction from a resistively heated tantalum foil pressed between the sample and a second identical piece of Ge that acted as a dummy sample by low thermal expansion ceramic bars fastened to a transferrable molybdenum sample carrier [35]. The temperature was measured using a *K*-type thermocouple attached to the surface of the dummy sample using a ceramic adhesive. Surfaces suitable for STM measurements were prepared by cycles of $Ar^+$ sputtering and annealing at 920 K until impurities were below the AES detection limit, followed by deposition of a 20-nm-thick Ge buffer layer deposited at 620 K and annealed at 920 K. This procedure produces low-defect-density surfaces with evenly spaced monatomic steps with the terrace widths governed by the misorientation of the wafer [36]. Strontium was deposited at 675 K and the surface was subsequently flashed to 900 K to obtain better order in the surface layer. The Sr coverage for the structures discussed in this work was 3/16 ML as monitored by both the QCM and AES.

All STM images were recorded at room temperature. Electrochemically etched tungsten STM tips were cleaned by electron beam bombardment prior to use. The tunneling current was 0.2 nA for all STM images. Throughout the paper, sample biases are reported so that negative biases probe occupied states and positive biases probe unoccupied states.

### B. Computational Details

The Sr/Ge system is modeled using first-principles density functional theory (DFT) calculations with a plane wave basis set and ultrasoft pseudopotentials [37–39]. A slab geometry with eight to ten layers of Ge and symmetric surfaces are used [40]. The generalized gradient approximation (GGA) is used to model the exchange correlation functional [41] and the method of Tersoff and Hamann is employed to simulate STM images [42,43]. It should be noted that the simulated empty-state STM images have different bias voltages compared to the corresponding experimental images. This phenomenon is due to the well-known fact that DFT underestimates band gaps under both the local density approximation (LDA) and the generalized gradient approximation (GGA) [44–46]. This is especially noticeable for Ge, whose band gap of 0.67 eV practically vanishes in our DFT calculations. Thus, it is difficult to compare directly the positive sample-bias voltages (empty states) in the STM data with those of calculated empty-state images, since their energy must be shifted upward by an unknown amount.

## III. RESULTS AND DISCUSSION

### A. Scanning tunneling microscopy observations

The general features of the 1D nanostructures that start to form on Ge(100) at Sr coverages above ∼1/16 ML are illustrated in Fig. 1. The filled-state STM image in Fig. 1(a) shows plateaus separated by trenches at regular intervals. The elevated plateaus are populated by elongated features arranged in rows along the direction of the trenches. Three-row-wide plateaus predominate; slightly higher coverages and longer annealing leads to almost exclusively three-row-wide plateaus [29]. The distance between the outer rows of the three-row-wide plateaus is six surface unit cells (6×) across both the plateaus and the trenches; thus, the overall structure is 12 substrate unit cells wide. In addition, the rows adjacent to the trenches appear 0.15 ± 0.1 Å higher.

Interestingly, the plateaus appear very differently in empty-state images such as Fig. 1(b). For this reverse bias, the areas adjacent to the trenches appear dim and the number of bright rows within each plateau is reduced by one compared to filled-state images. In addition, the features are now circular rather than elongated. These protrusions often exhibit shifts by one substrate unit cell within their rows, pointed to by the arrows in the figure, indicating a move to an equivalent site. Filled- and empty-state images of the same area [Figs. 1(c) and 1(d)] reveal additional curious details: First, the rows in the empty-state image are located in between those in the filled-state image, i.e., the bright features in the empty states appear dim in filled states, and vice versa; second, while the plateaus always appear symmetric in filled-state images, in empty-state images some of the plateaus appear asymmetric, with the central rows now different distances from the nearby trenches, as indicated by the marker in Fig. 1(d).

The finer details of the bias dependence are illustrated in the close-up images in Fig. 2. The filled-state image in Fig. 2(a) reveals that the middle row of the plateau is composed of elongated ovals that strongly resemble the building blocks of a lower-coverage (1/6 ML) (3 × 4) phase [47]. These central features are two substrate unit cells apart along $[01\bar{1}]$ and three unit cells from the outermost rows, resulting in a (6 × 2) arrangement atop the plateau. The bright features on the outer rows are often out of phase [as in Fig. 2(a)] with the central row as the plateaus are traversed in the [011] direction. While filled-state images are relatively insensitive to bias, empty-state images exhibit significant variations as the bias voltage is increased. At low positive bias [Fig. 2(b)] two

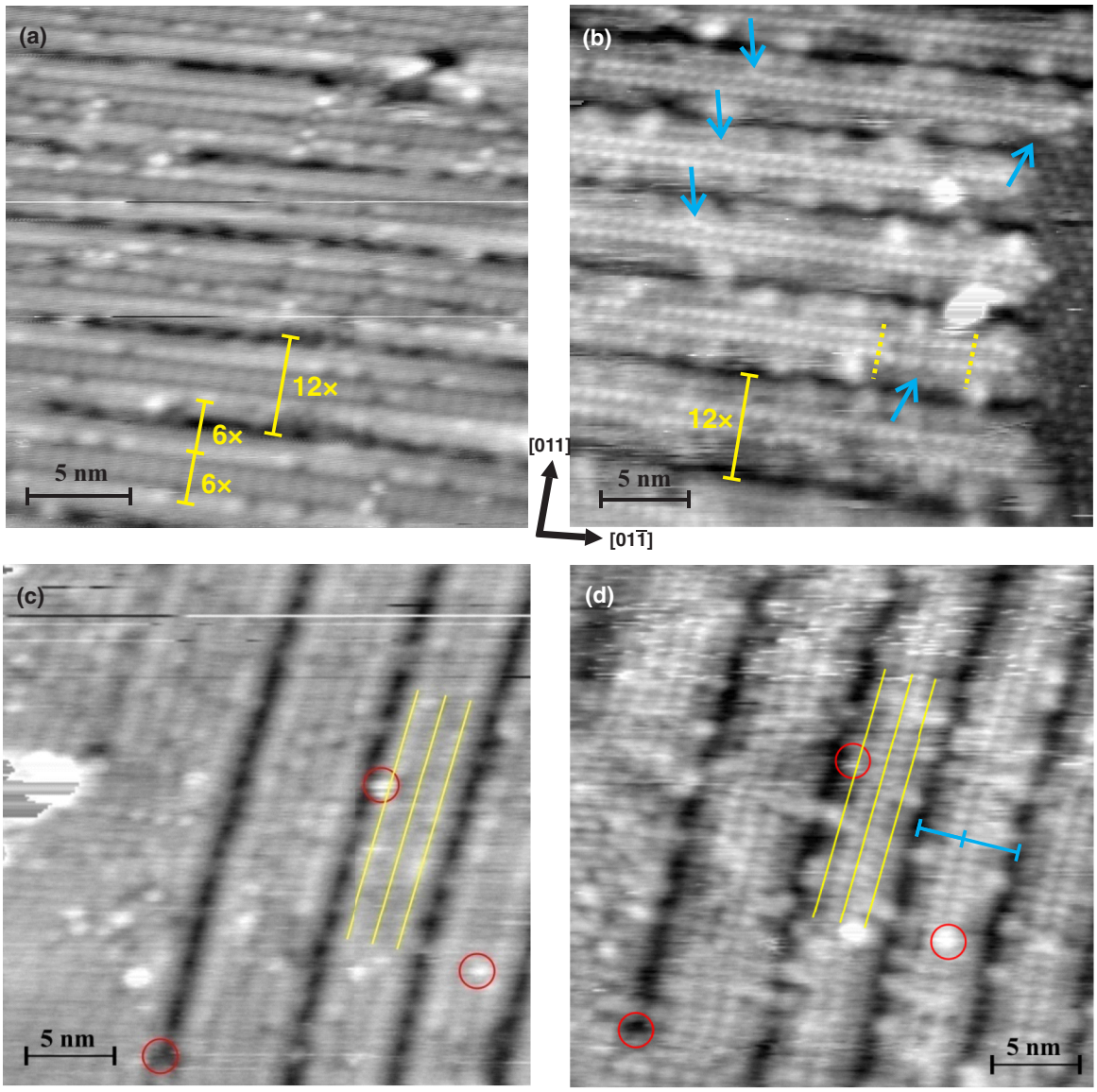


FIG. 1. (Color online) (a) Filled-state and (b) empty-state STM images of the plateau-trench structure at 3/16 ML Sr coverage. Characteristic distances are indicated in yellow. The blue arrows in (b) highlight places where the rows of white protrusions are further apart. (c) Filled- and (d) empty-state STM images of the same area on the surface. Red circles highlight the same features in the two images; yellow lines indicate the position of rows in the filled-state image in (c). Biases are −2.5 V (a), 1.25 V (b), −2 V (c), and 2 V (d).

rows of circular features 8 Å apart (2×) straddle the plateau center. Measurements reveal a 2 × periodicity [01$\bar{1}$] along the rows and [011] perpendicular to them. At higher positive bias [Fig. 2(c)] additional features appear halfway between the spots seen at the lower bias; meanwhile the original spots become more elongated along [01$\bar{1}$]. Additional features also appear near the edges of the plateau.

### B. Density functional theory calculations

The starting point for interpreting the complex geometrical and electronic structure revealed in the STM data is our detailed knowledge of the (3 × 4) Sr/Ge(100) phase that precedes the formation of stripes and trenches [47]. This phase covers the entire surface just below 1/6 ML Sr and can be seen at the right of Fig. 1(b) and the lower left of Fig. 1(c). Images of this (3 × 4) structure are also strongly bias dependent: Similar to the plateaus described above, features that appear bright in empty-state images appear dim in filled-state images, and for empty-state images, additional features appear at high bias [47]. We showed that these characteristics could be well reproduced by Sr atoms replacing two Ge dimers on the reconstructed Ge(100) surface. The building block for this structure, a Sr–double dimer vacancy complex, is the same one that produces a (3 × 2) structure on Si(100) [40], but with the blocks arranged in a staggered pattern on Ge(100) [47].

Based on our prior results, we again consider surface alloys. The most energetically stable configuration we found for the plateaus is pictured in Fig. 3. As shown in Fig. 3(a), its central building block is composed of a Sr atom (yellow) occupying the fourfold hollow between four Ge atoms (green) and two neighboring top-layer Ge dimers (light blue). This central

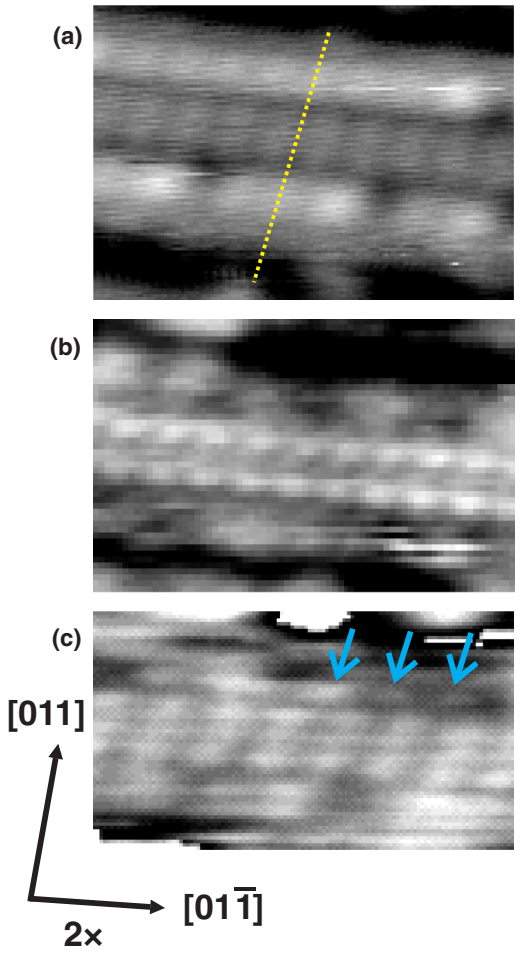


FIG. 2. (Color online) (a) Filled-state and (b), (c) empty-state close-up STM images of areas on the plateaus. The yellow dotted line runs through the center of features in the outer rows and in between features in the middle row. Arrows point to additional features in (c) compared to (b). Sample biases are −2.5 V (a), 1.25 V (b), 2 V (c).

building block is the same one that reproduces STM images of anti-phase-domain boundaries (APBs) in the lower-coverage $(3 \times 4)$ phase [47]. Second-layer Ge atoms (green) are exposed on either side of this central structure. Of the three hollow sites created, the middle is filled by a Sr atom, while the Ge atoms surrounding the others pair up to form dimers.

Since the STM images provide no insight into what is happening in the trenches, the modeling focuses on the plateaus; the trenches are approximated as pairs of bare Ge dimer rows one step down from the outermost Ge dimers on the plateaus. The result is a $(10 \times 2)$ structure as opposed to the observed $(12 \times 2)$ periodicity. The smaller unit cell reduces the required computation time, allowing us to test more structures while not sacrificing agreement with experiment (because the structure and composition of the trenches is unknown and because the width of the trench is sufficient to mitigate coupling between plateaus). In any event, the size of the imageable plateau area is $(6 \times 2)$. The Sr coverage in the plateau model in Fig. 3 is 3/16 ML, i.e., higher than the 1/6 ML Sr coverage in the $(3 \times 4)$ model, as expected. The actual surface coverage will depend on the composition of the trenches which could not be resolved

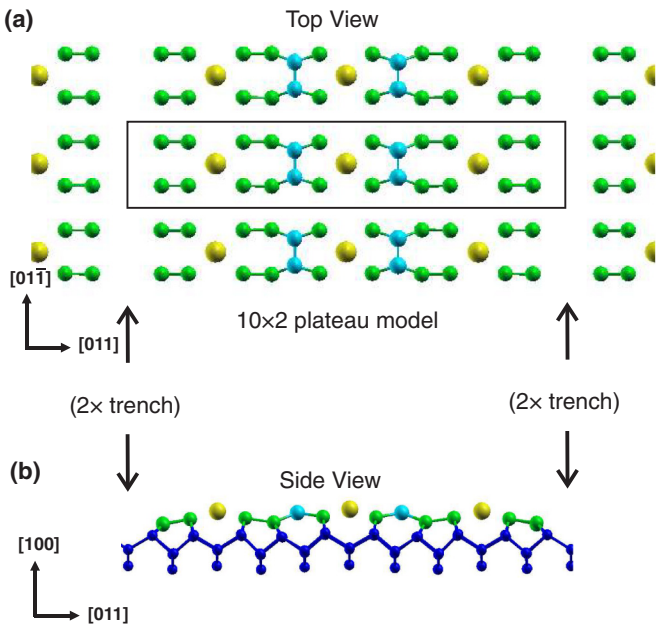


FIG. 3. (Color online) (a) Top and (b) side views of a $10 \times 2$ model of the plateau-trench structure. Sr: large yellow; top-layer Ge dimers: cyan; exposed surface Ge: green; bulk Ge: dark blue.

in the experiments. The approximation of the trenches as bare dimer rows translates into an overall coverage of 1/8 ML; since the total Sr coverage must be greater than 1/6 ML, the trenches must contain Sr.

Similar to our $(3 \times 4)$ model, the side view in Fig. 3(b) reveals significant distortion in the top Sr/Ge layer. The top-layer Ge dimers are contorted into an unusual nearly planar $sp^2$ bonding geometry rather than the typical Ge $sp^3$ tetrahedral configuration. This is consistent with our previous finding that substitution of Sr into Ge and Si(100) surfaces leaves the semiconductor atoms in the neighboring outermost dimer in a nearly planar configuration with a dangling bond state with strong $p_z$ character and an $sp^2$-like bonding scheme [40,47]. As illustrated in Fig. 4, simulated STM images of this structure show agreement with the trends observed in the experiment. Below the Fermi level, all simulated images appear similar to Fig. 4(b) with broader maxima in the middle extending over the Sr all the way to the neighboring Ge dimers, and narrower maxima at the outer rows over the Sr and its four neighboring Ge atoms, consistent with experiment. The broad maxima in the middle are associated with the passivated dangling bond states due to electron transfer from the Sr atoms and the $p_z$-like states of the top-layer Ge dimers (light blue) to the surrounding second-layer Ge (green), while the narrower maxima near the plateau edges are due to passivation by Sr only. In contrast to filled-state images, above the Fermi level simulated images reveal a strong bias dependence, again consistent with experiment. At low positive bias [Fig. 4(c)], the contrast is dominated by the $p_z$-like states centered on the top-layer Ge dimers. At high positive bias [Fig. 4(d)], the tunneling probability to the Sr $s$ and $d$ empty orbitals increases, resulting in the additional features centered on the Sr atoms. In addition, the Ge $p_z$-like empty states appear more elongated, also in accord with experiment.

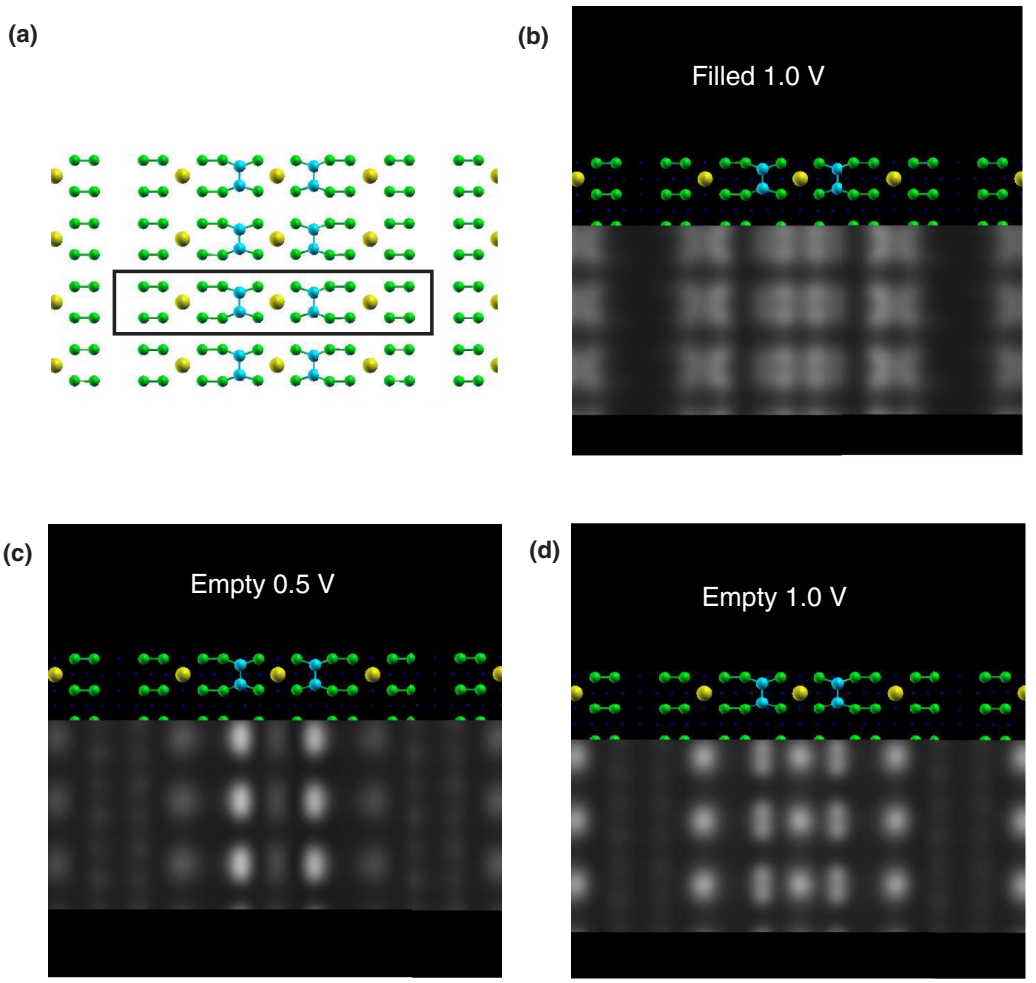


FIG. 4. (Color online) (a) The 10 × 2 structure with the unit cell highlighted by the box. (b)–(d) Simulated STM images of the model.

One noticeable difference between theory and experiment, besides the lower resolution of the experiments, is the lack of higher intensity in the rows alongside the trenches. This is not surprising given the lack of experimental information on the trenches that led us to approximate the trenches as bare Ge dimer rows. For the same reason, it is difficult to compare the energy of our plateau model to other possible structures. We did, however, calculate the energy of a (6 × 2) model as a continuous repeat of the plateau structure without the trenches. We found that it is only 0.024 eV/Sr less stable than the ground state (3 × 4) phase, and significantly more energetically favorable than any adatom models that could match the experimental data.

Another feature of our plateau-trench model is that it can easily accommodate the various defects within the plateau structure observed in Figs. 1 and 2 above. The 1 × shifts observed perpendicular to the plateaus in low-bias empty-state images [arrows in Fig. 1(b)] can be accounted for by the topmost-layer Ge dimers moving from the sites next to the center Sr atoms to nearly equivalent sites next to the outer Sr atoms, as pictured in Fig. 5(a). When several Ge dimers shift to sites next to the outer Sr atoms, we obtain an asymmetric structure in empty-state images, where the bright features centered on the outermost Ge dimers (shaded circles in Fig. 5(a)) are closer to one trench compared to the other. In contrast, filled-state features that are centered on the Sr atoms remain symmetric relative to the trenches, consistent with experiment. We also consider a plateau model in which the outer Sr rows are shifted by one lattice constant along the trench [Fig. 5(b)]. This structure is energetically the same as the model in Figs. 3 and 4 except that the outer features in the simulated images are now out of phase with the maxima in the center rows, as observed in some experimental images.

### C. Model validation

A somewhat puzzling feature of the structural model proposed here is that the topmost-layer Ge dimer rows (light blue) run perpendicular to the kink-free trenches, which can be viewed as step edges, as well as to descending steps to the lower-coverage (3 × 4) structure that appear very straight [29]. It is well known that descending steps perpendicular to the dimer rows on (2 × 1)-reconstructed semiconductor (100) surfaces are high-energy $S_B$ steps that have rough edges, while descending steps parallel to the dimer rows are low-energy $S_A$ steps with very straight edges [48]. This discrepancy prompted us to calculate the step energies for our models. Our results indicate that it is the exposed second-layer Ge dimers (green dimers) in both the plateau model presented here and the (3 × 4) structure discussed previously that are important for step

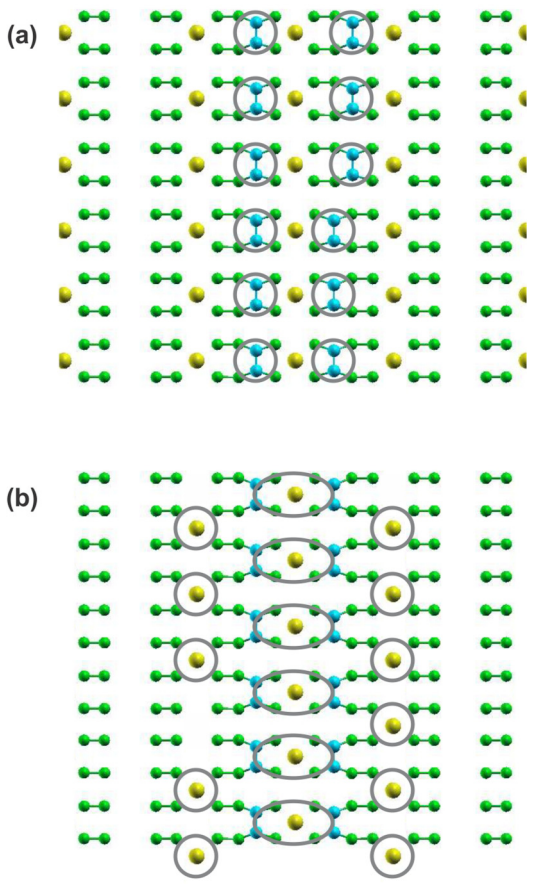


FIG. 5. (Color online) Models of some common defect structures on the plateaus. Color scheme as in Fig. 3. (a) A defect formed by shifting topmost Ge dimers one lattice spacing to the right. The circles highlight the bright features seen in empty-state STM images. (b) A defect formed by shifting the Sr rows next to the trenches by one lattice constant. One Sr atom on the left is missing. The circles and ellipses correspond to features seen in filled-state STM images.

energetics. Thus, the low-energy steps have the second-layer Ge dimers parallel to the descending straight step edge, as shown schematically in Fig. 6. This is consistent with step formation on bare Ge surfaces where dimer rows parallel

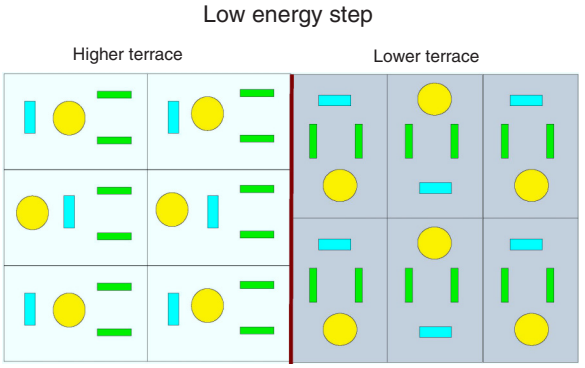


FIG. 6. (Color online) A schematic of a low-energy step for the 3 × 4 structure. Sr: yellow; top-layer Ge dimers: cyan; exposed second-layer Ge dimers: green.

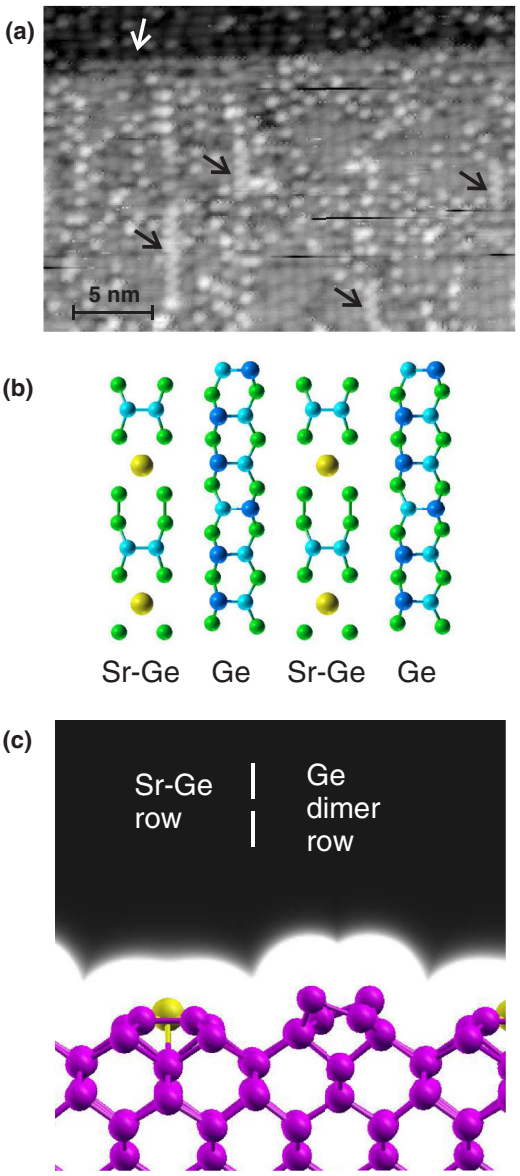


FIG. 7. (Color online) (a) Filled-state (–1.75 V) STM image of the Ge surface after depositing 1/8 ML of Sr. Arrows point to buckled Ge dimer rows within the 3 × 4 phase. (b) A model of the surface with alternating (3 × 2) 1/6 ML blocks and Ge dimer rows running along the 3 × direction; Sr: yellow; top-layer flat Ge dimers: cyan; raised buckled Ge dimer: dark blue. (c) A side view of the (3 × 2) unit and a dimer row highlighting the height difference. The background colors indicate the maximum value along the $y$ direction (into the paper) of the local density of states, integrated from −1 eV to the Fermi level. Sr: yellow; Ge: purple.

straight $S_A$ step edges, and agrees with our experimental data for the plateau-trench phase and for the lower-coverage (3 × 4) phase where the exposed second-layer dimer rows parallel the straight step edges.

The picture outlined above is supported by experimental observations and further calculations. In the filled-state STM image in Fig. 7(a), the Sr coverage is slightly less than 1/8 ML. At this coverage the surface is covered by the (3 × 4) phase and occasional unidentified white circular protrusions [29].

We also note the formation of short rows on the surface [pointed to by the arrows in Figure 7(a)] which exhibit the unmistakable buckling of Ge dimer rows. Surprisingly, these dimer rows run along the 3 × direction of the (3 × 4) structure and perpendicular to the straight step edge at the top of the image. Height profile measurements indicate that the buckled Ge dimer rows are 0.8 ± 0.1 Å higher than the elongated building blocks of the (3 × 4) structure surrounding them. These numbers are too low for adsorbed Ge atop the (3 × 4) phase. Therefore, we constructed a model in which a bare Ge dimer row is incorporated into the structure next to the Sr–double dimer vacancy building units of the 1/6 ML structure [Fig. 7(b)] and calculated the height difference expected in STM images. The calculations indicate that this is a stable arrangement, only 0.1 eV/Sr higher in energy than the (3 × 4) phase. In this model, the raised buckled Ge dimer is 0.75 Å above the Sr atoms, and the pure Ge dimer row appears consistently higher in simulated filled-state images [Fig. 7(c)], in agreement with the experimental measurements. These results define the crystallographic direction of the surface (i.e., the dimer orientation) and clearly show that the low-energy step direction in Sr-substituted Ge surfaces is governed not by the orientation of the topmost Ge dimers but by those one layer down. This is unambiguously supported by the presence of a gray, buckled Ge dimer row paralleling the edge in Fig. 7(a), as highlighted by the white arrow.

### D. Higher-coverage Sr/Ge structures

We previously reported that the trenches, which are predominantly 12 unit cells apart at the 3/16 ML Sr coverage discussed above, become more ordered and more closely spaced as the Sr coverage increases: they are 9 unit cells apart at ≈1/4 ML of Sr and become 6 unit cells apart near 3/4 ML Sr coverage [29]. While this 12× → 9× → 6× sequence of trench spacings shows a clear trend with increasing Sr coverage, it is difficult to determine its origin since STM does not provide any insight into the composition of the trenches. The formation of trenches on the surface, however, can be associated with strain relief [29]. The inclusion of the larger Sr atoms in a surface alloy constrained to match the bulk Ge underneath leads to compressive strain, and the trenches provide space for the surface layer to relieve this strain. In this regard, it is not surprising that the trench spacings become smaller as the Sr coverage increases.

We also considered thermodynamically stable structures around 0.5 ML of Sr on Ge. Unlike Sr on Si, which features a stable (2 × 1) adlayer structure at 0.5 ML Sr coverage [36], we find that the Sr/Ge system does not form a thermodynamically stable structure at this coverage; instead the system will phase separate into the 1/6 ML structure and a higher-coverage structure [49]. This is consistent with the diffraction and STM data that do not reveal an ordered phase at 1/2 ML Sr coverage on Ge [29].

One explanation for this difference between Si and Ge is revealed in Table I, which shows the calculated energies and characteristic Sr-Ge and Sr-Si bond lengths for the 1/6 and 1/2 ML Sr/Ge and Sr/Si structures. Comparison of the values in the last column indicates that the Sr bond lengths for the preferred 1/6 ML structures on Ge and Si—(3 × 4) and (3 × 2), respectively—are almost identical (3.25 Å vs 3.26 Å). At 1/2 ML Sr, the Si-Sr distance in the stable (2 × 1) configuration is also very similar: 3.31 Å. The Ge-Sr distance in the equivalent structure, however, is 3.43 Å, resulting in much weaker overlap between the Sr and Ge orbitals. In fact, all thermodynamically stable Sr/Ge structures have average Sr-Ge distances between 3.18 and 3.25 Å, which are shorter than any of the Ge-Sr distances for dimerized surfaces such as the (2 × 1) 1/2 ML Sr surface. The larger Ge lattice constant (0.16 Å larger surface lattice constant compared to Si) provides a logical explanation for this trend.

TABLE I. Energies and characteristic distances for 1/6 and 1/2 ML Sr-induced structures on Ge(001) and Si(001).

| Substrate | Sr coverage (ML) | Unit cell | Vacancies (ML) | $E_{bind}$ (eV/Sr) | Sr bond (Å) |
|---|---|---|---|---|---|
| Ge | 1/6 | 3 × 4 | 2/3 | 3.54 | 3.25 |
| Ge | 1/2 | 2 × 1 | 0 | 3.29 | 3.43 |
| Si | 1/6 | 3 × 2 | 2/3 | 3.90 | 3.26 |
| Si | 1/2 | 2 × 1 | 0 | 3.53 | 3.31 |

## IV. CONCLUSIONS

The details of Sr-induced nanostructuring of the Ge(100) surface into ordered arrays of trenches and plateaus have been examined using scanning tunneling microscopy and density functional theory. Atomic-resolution images of the plateaus exhibit dramatic bias dependence in STM that is explained with the help of first-principles calculations of energetically favorable structures. The lowest-energy structures found involve Sr replacing Ge dimers creating a surface alloy; simulated STM images of such structures reproduce well the experimental data. In particular, the simulated filled-state images emphasize the positions of Sr-Ge bonds, while empty-state images near $E_F$ emphasize the topmost Ge dimers with an increasing contribution from the Sr atoms as the bias was increased. These findings reproduce the contrast reversal observed experimentally when the polarity of the bias voltage is flipped, as well as the appearance of new features in empty images obtained at high biases. Although the atomic level details of the bottom of the trenches remains elusive, the structural model explains the unusual finding that the almost perfectly straight trench edges run perpendicular to the topmost Ge dimer rows, the opposite of what is almost always seen on semiconductor (100) surfaces. We show that Sr incorporation into the surface leaves Ge dimer rows parallel to the trench edge but one layer below the topmost dimers, explaining this unusual phenomenon. Higher-Sr-coverage structures are also investigated, and in contrast to Si, Ge(100) not only favors the formation of ordered nanostrips and trenches on the surface, but also lacks stable structures at 0.5 ML of Sr, which are key to successful epitaxy on Si(100). In contrast to Si(100) where a flat (2 × 1) ultimately forms when the Sr coverage is increased, on Ge the trenches become more ordered and move closer together when the coverage is increased. While the Sr/Si (2 × 1) structure is useful for oxide epitaxy, the self-organization of the Ge surface into plateaus and trenches driven by strain

relief can be potentially useful for device self-assembly and basic science experiments on 1D phenomena.

## ACKNOWLEDGMENTS

This work was supported by the National Science Foundation through the Yale Materials Research Science and Engineering Center, Grant No. DMR-1119826. B.R.L. and E.I.A. acknowledge the help of M. Li and M. Herdiech in carrying out the experiments. Computational facilities were supported by NSF Grant No. CNS 08-21132 and by the facilities and staff of the Yale University Faculty of Arts and Sciences High Performance Computing Center. Additional computations were carried out via the NSF XSEDE resources through Grant No. TG-MCA08X007.

[1] P. M. Mooney and J. O. Chu, Annu. Rev. Mater. Sci. **30**, 335 (2000).
[2] S. Nakaharai, T. Tezuka, N. Sugiyama, Y. Moriyama, and S. Takagi, Appl. Phys. Lett. **83**, 3516 (2003).
[3] O. G. Schmidt and K. Eberl, IEEE Trans. Electron Devices **48**, 1175 (2001).
[4] T. Mizuno, N. Sugiyama, T. Tezuka, T. Numata, and S. Takagi, IEEE Trans. Electron Devices **50**, 988 (2003).
[5] O. Gurlu, O. A. O. Adam, H. J. W. Zandvliet, and B. Poelsema, Appl. Phys. Lett. **83**, 4610 (2003).
[6] J. Wang, M. Li, and E. I. Altman, Phys. Rev. B **70**, 233312 (2004).
[7] M. Fischer, A. van Houselt, D. Kockmann, B. Poelsema, and H. J. W. Zandvliet, Phys. Rev. B **76**, 245429 (2007).
[8] A. A. Stekolnikov, F. Bechstedt, M. Wisniewski, J. Schäfer, and R. Claessen, Phys. Rev. Lett. **100**, 196101 (2008).
[9] J. Wang, M. Li, and E. I. Altman, Surf. Sci. **596**, 126 (2005).
[10] A. Van Houselt, D. Kockmann, T. F. Mocking, B. Poelsema, and H. J. W. Zandvliet, Phys. Rev. Lett. **103**, 209702 (2009).
[11] R. Niikura, K. Nakatsuji, and F. Komori, Phys. Rev. B **83**, 035311 (2011).
[12] J. Schäfer, C. Blumenstein, S. Meyer, M. Wisniewski, and R. Claessen, Phys. Rev. Lett. **101**, 236802 (2008).
[13] D. E. P. Vanpoucke and G. Brocks, Phys. Rev. B **81**, 085410 (2010).
[14] A. van Houselt, M. Fischer, B. Poelsema, and H. J. W. Zandvliet, Phys. Rev. B **78**, 233410 (2008).
[15] M. Kageshima, Y. Torii, Y. Tano, O. Takeuchi, and A. Kawazu, Surf Sci. **472**, 51 (2001).
[16] H. Itoh, S. Narui, A. Sayama, and T. Ichinokawa, Phys. Rev. B: Condens. Matter **45**, 11136 (1992).
[17] J. W. Reiner, A. M. Kolpak, Y. Segal, K. F. Garrity, S. Ismail-Beigi, C. H. Ahn, and F. J. Walker, Adv. Mater. **22**, 2919 (2010).
[18] C. H. Ahn, K. M. Rabe, and J. M. Triscone, Science **303**, 488 (2004).
[19] C. H. Ahn, J. M. Triscone, and J. Mannhart, Nature **424**, 1015 (2003).
[20] T. P. Ma and J.-P. Han, IEEE Electron Device Lett. **23**, 386 (2002).
[21] R. A. McKee, F. J. Walker, and M. F. Chisholm, Phys. Rev. Lett. **81**, 3014 (1998).
[22] R. A. McKee, F. J. Walker, and M. F. Chisholm, Science **293**, 468 (2001).
[23] H. Mori and H. Ishiwara, Jpn. J. Appl. Phys., Part 2 **30**, 1415 (1991).
[24] Y. Liang, S. Gan, and M. Engelhard, Appl. Phys. Lett. **79**, 3591 (2001).
[25] J. Lettieri, J. H. Haeni, and D. G. Schlom, J. Vac. Sci. Technol. A **20**, 1332 (2002).
[26] H. Xiaoming, Z. Yu, J. Curless, R. Droopad, K. Eisenbeiser, J. Edwards, W. Ooms, and D. Sarid, Appl. Surf. Sci. **181**, 103 (2001).
[27] W. Du, B. Wang, L. Xu, Z. Hu, X. Cui, B. C. Pan, J. Yang, and J. G. Hou, J. Chem. Phys. **129**, 164707 (2008).
[28] H. Jiehui, Z. Guanhua, G. Jiandong, G. Qinlin, and W. Kehui, J. Appl. Phys. **109**, 083522 (2011).
[29] B. R. Lukanov, J. W. Reiner, F. J. Walker, C. H. Ahn, and E. I. Altman, Phys. Rev. B **84**, 075330 (2011).
[30] C. J. Först, C. R. Ashman, K. Schwarz, and P. E. Blöchl, Nature **427**, 53 (2004).
[31] X. Zhang, A. A. Demkov, H. Li, X. Hu, Y. Wei, and J. Kulik, Phys. Rev. B **68**, 125323 (2003).
[32] P. W. Peacock and J. Robertson, Appl. Phys. Lett. **83**, 5497 (2003).
[33] A. M. Kolpak, F. J. Walker, J. W. Reiner, Y. Segal, D. Su, M. S. Sawicki, C. C. Broadbridge, Z. Zhang, Y. Zhu, C. H. Ahn, and S. Ismail-Beigi, Phys. Rev. Lett. **105**, 217601 (2010).
[34] A. M. Kolpak and S. Ismail-Beigi, Phys. Rev. B **85**, 195318 (2012).
[35] C. Y. Nakakura, V. M. Phanse, G. Zheng, G. Bannon, E. I. Altman, and K. P. Lee, Rev. Sci. Instrum. **69**, 3251 (1998).
[36] L. H. Chan, E. I. Altman, and Y. Liang, J. Vac. Sci. Technol. A **19**, 976 (2001).
[37] P. Hohenberg and W. Kohn, Phys. Rev. **136**, B864 (1964).
[38] W. Kohn and L. J. Sham, Phys. Rev. **140**, A1133 (1965).
[39] D. Vanderbilt, Phys. Rev. B: Condens. Matter **41**, 7892 (1990).
[40] K. Garrity and S. Ismail-Beigi, Phys. Rev. B **80**, 085306 (2009).
[41] J. P. Perdew, K. Burke, and M. Ernzerhof, Phys. Rev. Lett. **77**, 3865 (1996).
[42] J. Tersoff and D. R. Hamann, Phys. Rev. Lett. **50**, 1998 (1983).
[43] J. Tersoff and D. R. Hamann, Phys. Rev. B **31**, 805 (1985).
[44] J. P. Perdew and M. Levy, Phys. Rev. Lett. **51**, 1884 (1983).
[45] J. P. Perdew, R. G. Parr, M. Levy, and J. L. Balduz, Jr., Phys. Rev. Lett. **49**, 1691 (1982).
[46] L. J. Sham and M. Schlüter, Phys. Rev. Lett. **51**, 1888 (1983).
[47] B. Lukanov, K. Garrity, S. Ismail-Beigi, and E. I. Altman, Phys. Rev. B **85**, 195316 (2012).
[48] H. J. W. Zandvliet, Phys. Rep. **388**, 1 (2003).
[49] K. F. Garrity, Ph.D. thesis, Yale University, 2011.